drones

MDPI

Article

Integration of UAV Digital Surface Model and HEC-HMS Hydrological Model System in iRIC Hydrological Simulation—A Case Study of Wu River

Yen-Po Huang [1], Hui-Ping Tsai [1,2,3,4,*] and Li-Chi Chiang [5]

[1] Department of Civil Engineering, National Chung Hsing University, Taichung 402, Taiwan; matt94082@gmail.com
[2] Innovation and Development Center of Sustainable Agriculture, National Chung Hsing University, Taichung 402, Taiwan
[3] i-Center for Advanced Science and Technology (i-CAST), National Chung Hsing University, Taichung 402, Taiwan
[4] Smart Multidisciplinary Agriculture Research and Technology Center, National Chung Hsing University, Taichung 402, Taiwan
[5] Department of Bioenvironmental Systems Engineering, National Taiwan University, Taipei 10617, Taiwan; lchiang@ntu.edu.tw
* Correspondence: huiping.tsai@nchu.edu.tw

Abstract: This research investigates flood susceptibility in the mid- and downstream areas of Taiwan's Wu River, historically prone to flooding in central Taiwan. The study integrates the Hydrologic Engineering Center—Hydrologic Modeling System (HEC-HMS) for flow simulations with unmanned aerial vehicle (UAV)-derived digital surface models (DSMs) at varying resolutions. Flood simulations, executed through the International River Interface Cooperative (iRIC), assess flood depths using diverse DSM resolutions. Notably, HEC-HMS simulations exhibit commendable Nash–Sutcliffe efficiency (*NSE*) exceeding 0.88 and a peak flow percentage error (*PEPF*) below 5%, indicating excellent suitability. In iRIC flood simulations, optimal results emerge with a 2 m resolution UAV-DSM. Furthermore, the study incorporates rainfall data at different recurrence intervals in iRIC flood simulations, presenting an alternative flood modeling approach. This research underscores the efficacy of integrating UAV-DSM into iRIC flood simulations, enabling precise flood depth assessment and risk analysis for flood control management.

Keywords: UAV; DSM; flood simulation; HEC-HMS; iRIC

check for updates

Citation: Huang, Y.-P.; Tsai, H.-P.; Chiang, L.-C. Integration of UAV Digital Surface Model and HEC-HMS Hydrological Model System in iRIC Hydrological Simulation—A Case Study of Wu River. *Drones* **2024**, *8*, 178. https://doi.org/10.3390/drones8050178

Academic Editor: Higinio González Jorge

Received: 20 March 2024
Revised: 21 April 2024
Accepted: 25 April 2024
Published: 30 April 2024

1. Introduction

As global warming intensifies, the intensity and frequency of extreme rainfall events are increasing in monsoon regions worldwide. The Asian monsoon region is particularly vulnerable to extreme rainfall events induced by rising temperatures, as noted by [1,2]. Such extreme rainfall events can lead to various disasters, including floods, droughts [3], and landslides [4]. These events not only cause significant economic damage [5], but also inflict irreversible harm on ecosystems [6]. According to the United Nations Emergency Events Database (EM-DAT), floods constituted approximately 45% of major natural disasters from 2002 to 2021, accounting for about 22% of the total economic losses.

Taiwan, located in the East Asian monsoon region, receives abundant rainfall. However, due to the island's rugged topography, characterized by short and rapidly flowing rivers, this rainfall is unevenly distributed both spatially and temporally [7]. In 2005, the World Bank recognized Taiwan as a country vulnerable to compound disasters, with floods caused by heavy rainfall being the most common [8]. Numerous climate studies have shown that in recent decades, both the intensity and frequency of extreme rainfall events in Taiwan have increased noticeably [9–11] leading to a corresponding rise in flood risk [12].

Hydraulic analysis software and models are widely used to study the causes and impacts of flooding, as well as related hydrological issues [13]. These models are generally classified into three types: 1D (one-dimensional), 2D (two-dimensional), and hybrid models that integrate 1D and 2D methodologies. The combination of 1D and 2D models not only improves computational efficiency, but also effectively assesses the extent of flood events [14–16].

The Hydrologic Engineering Center—Hydrologic Modeling System (HEC-HMS), developed by the U.S. Army Corps of Engineers, is a versatile hydrological model. It is widely used for urban drainage, spillway design in reservoirs, floodplain management, wetland hydrology, flood warning systems, stream restoration, flow prediction, surface erosion, and other hydrological applications [17,18]. Ref. [19] employed HEC-HMS in conjunction with GIS data for flow simulations on Lagos Island, Nigeria, aiding in the development of a local flood warning system. Ref. [20] used HEC-HMS to study the impact of urbanization on river flow in Poland's Wirynka River Basin, revealing a significant increase in flow due to urban development. In Taiwan, Ref. [21] utilized HEC-HMS for flood simulation in Kaohsiung City, creating flood depth and range maps for various recurrence intervals and assessing flood risks. Additionally, Ref. [22] conducted long-term flow simulations in the Gaoping River Basin between 2016 and 2018, contributing valuable insights for local water resource management and planning.

The International River Interface Cooperative (iRIC), established in 2007 by Professor Yasuyuki Shimizu of Hokkaido University and Dr. Jonathan Nelson from the United States Geological Survey (USGS), primarily focuses on flood simulation [23]. Ref. [24] evaluated flood-prone areas in Kabul, Afghanistan, using iRIC with a 90 m resolution digital elevation model (DEM). They adjusted the elevation data along the river due to the DEM's limited resolution, which improved the simulation results and identified river overflow as the main cause of flooding. iRIC has been coupled with other hydrological models in various studies [25,26]. For instance, Ref. [26] integrated HEC-HMS with iRIC using a 30 m resolution DEM from USGS to map flood risks in Sri Lanka's Nilwala River in May 2017, and [26] combined the Soil and Water Assessment Tool (SWAT) with iRIC to simulate a major flood event in India's Periyar River basin, providing insights for flash flood planning and management, including scenarios with and without dam spillway operations. While iRIC has been utilized in various countries, including Japan [27], Thailand [28], Morocco [29], Indonesia [30], Rwanda [31], and Ghana [32], its application in Taiwan remains relatively limited.

Remote sensing data and hydrological models are crucial for simulating and predicting flood disasters caused by rivers, significantly improving the accuracy and efficiency of flood disaster mapping and forecasting [33]. However, the lower resolutions of publicly available DEMs often present limitations, especially in small-scale flood simulations [34]. This is particularly challenging for small-scale basins or tributaries, where detailed geographical data may be lacking, complicating the construction of accurate models and the implementation of effective flood management strategies. The uncertainty in disaster prevention strategies is further increased by these limitations. Terrain is a primary determinant of surface runoff following rainfall events and plays a critical role in the accuracy of flood models [5].

In recent years, the rapid advancement of unmanned aerial vehicle (UAV) technology has provided an economically cost-effective means to acquire high-resolution orthoimages, DEMs, and DSMs [35–37]. Numerous studies have successfully utilized UAVs for hydrological simulations. For instance, Ref. [38] evaluated the flood prediction capabilities of a UAV-produced DEM with a 0.25 m resolution in a small tributary of the Marta River in central Italy. Ref. [39] compared the performance of various public DEMs in simulating flood extents in the Biga River basin in Turkey, using UAV-produced DEMs as a benchmark. Ref. [40] employed UAVs to generate DSMs at different resolutions and satellite images to estimate flooded areas in South Korea, demonstrating the significant value of UAVs in flood assessment. In Taiwan, scholars have also embraced UAVs for hydrological research. Studies such as those in [12,41] have utilized UAVs to model river depth and simulate flood ranges, contributing to enhanced disaster prevention and management in both mountainous and urban areas.

This research aims to leverage the capabilities of UAVs to generate high-resolution DSMs for small-scale flood simulations. The Wu River basin in central Taiwan, known for its susceptibility to flooding, especially in the downstream regions, was selected for this study. This area has experienced multiple flooding incidents in recent years, with the most significant event occurring on 20 May 2019. This heavy rainfall event, attributed to frontal influences, resulted in substantial rainfall across Taiwan, particularly in the northern and central regions. Notably, the Taichung weather station recorded a peak hourly rainfall of 82 mm, leading to flooding in various parts of Taichung City. The study aims to enhance flood depth estimation and management in the Wu River basin through the following research objectives: (1) utilizing HEC-HMS to simulate heavy rain and typhoon-induced river flow and establishing an iRIC hydraulic model; (2) employing UAV technology to create high-precision DSMs with varying resolutions and assessing their impact on predicting flood depths using hydraulic models; (3) conducting an analysis of rainfall recurrence intervals and flood simulations to identify areas at higher risk of flooding within the simulation scope.

2. Materials and Methods

2.1. Study Area

This research focused on the mid- and downstream of the Wu River basin, encompassing an area of approximately 612.6 km^2 (Figure 1). The Wu River basin is situated along Taiwan's central-western coast, spanning Taichung City, Changhua County, and Nantou County. It is bounded by the Central Mountain Range to the east, the Dajia River basin to the north, the Taiwan Strait to the west, and the Zhuoshui River basin to the south. The basin extends approximately 84 km from east to west and 52 km from north to south, with a main stream length of around 119.13 km and a total basin area of roughly 2025.6 km^2, characterized by an average slope of 0.0109. Figure 1b shows a 24 h 650 mm potential inundation map of the UAV coverage at various depths of 0.3–0.5 m, 0.5–1 m, 1–2 m, 2–3 m, and >3 m.

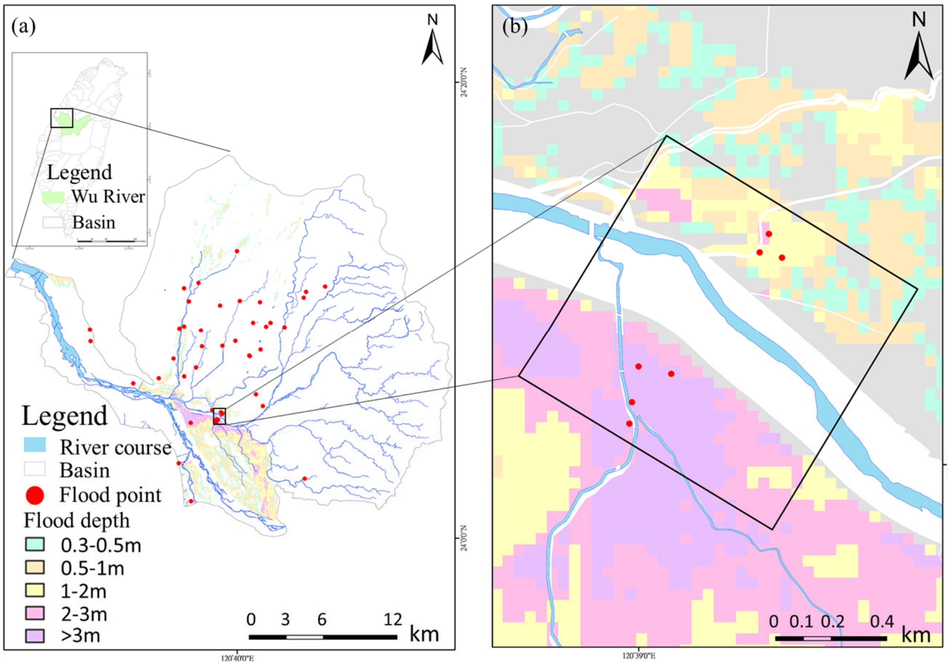

Figure 1. The research area includes (**a**) the distribution of river basins in Taiwan, flood points in the past five years, and a 24 h 650 mm potential inundation map of the study area, and (**b**) spatial coverage of UAV aerial photography. The various potential inundation depths of 0.3–0.5 m, 0.5–1 m, 1–2 m, 2–3 m, and >3 m are color–coded.

On 20 May 2019, heavy rainfall in Taiwan led to the identification of 242 flood points and caused losses exceeding TWD 1.6 billion, with severe flooding in areas such as Wuguang Village in Wuri District and Wufu Village in Wufeng District of Taichung City. Additionally, an analysis of inundation potential and flood hotspots from 2017 to 2021 has classified this region as a high-risk inundation zone within the Wu River basin. Consequently, this area was selected as the primary focus for UAV aerial photography in the study. The research involved using HEC-HMS simulations to model the river flow induced by heavy rainfall, employing UAVs to gather geographic data for constructing a high-precision DSM and integrating this data into iRIC for flood simulations to accurately replicate the extent and depth of the flooding.

2.2. Materials

In this study, various data types were collected, including rainfall, DEM, soil, and land use information (Figure 2). Rainfall data for the middle and lower sections of the Wu River basin were obtained from the Central Weather Administration (CWA). The Water Resources Agency (WRA) provided flow data and cross-sectional data. The Department of Land Administration (LDA) supplied elevation data in the form of a 20 m resolution DEM, which was created in 2017. ArcGIS was utilized for slope calculations. The terrain of the research area is characterized by flat topography in the western half and steep terrain in the eastern half, with elevations reaching as high as 1203 m.

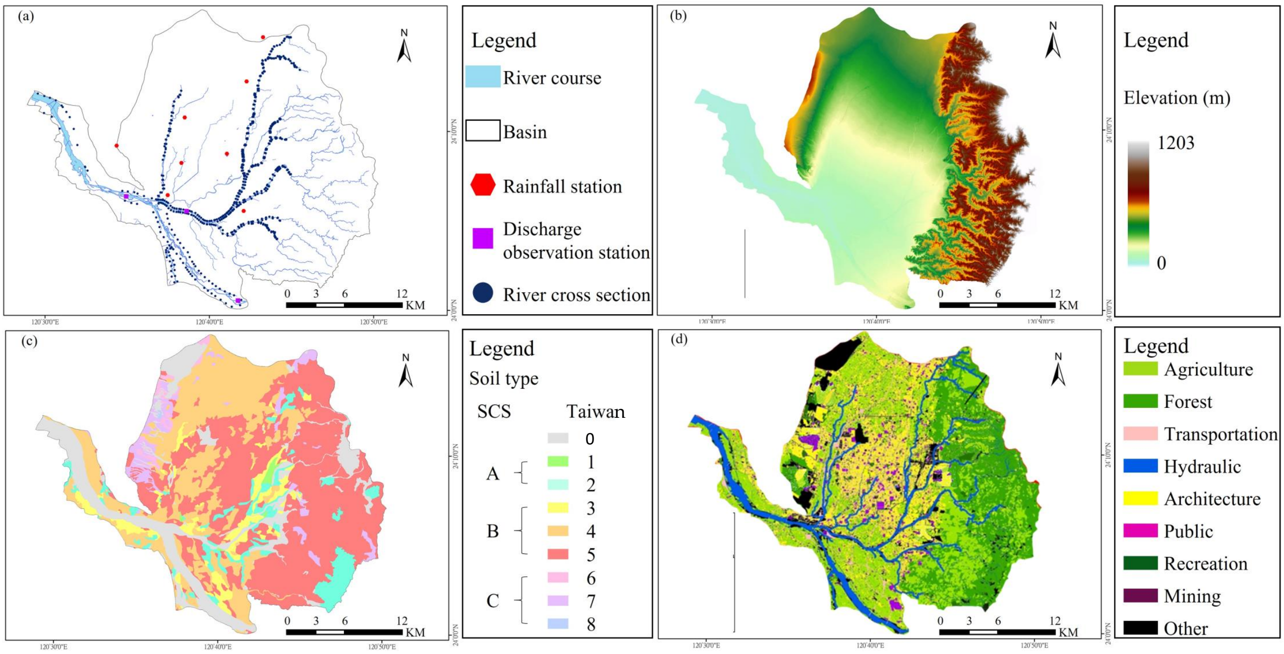

Figure 2. Research materials: (**a**) distribution map of rainfall stations, discharge observation stations, river cross sections, and river cross section piles; (**b**) topographic map; (**c**) surface soil classification map; (**d**) land use/land cover distribution map.

Soil data were procured from the Taiwan Agricultural Research Institute (TARI). Soil classification followed the U.S. Soil Conservation Service (SCS) system, which categorizes soil into three types. Additionally, TARI classified the topsoil into ten categories based on texture. The predominant topsoil texture in the study area fell within categories 3 to 6 (Class B), representing 74.4% of the area. Land use and land cover (LULC) data were based on survey results conducted by the National Land Surveying and Mapping Center (NLSC) in 2020. The western portion of the study area is primarily used for agriculture and urban development, while the eastern part is predominantly covered by forests.

To overcome the challenges posed by the dense building coverage in the study area and the necessity of adequate airspace, we utilized the DJI Phantom 4 Pro Quad-rotor

UAV for aerial imaging. This UAV was deployed to capture detailed images of the study area, enabling the creation of a DSM. The data collection process encompassed three flight missions, with four specific flights conducted over the heavily flooded regions of Wuguang Village in Wuri District and Wufu Village in Wufeng District. These flights covered areas ranging from 1.6 to 1.74 km^2.

However, it is important to note that the flight mission scheduled for 28 March was only partially completed due to adverse weather conditions and limited daylight hours. The remaining tasks were successfully completed on 6 April. In contrast, the flight missions on 3 May and 12 June were both accomplished within their respective scheduled days (Table 1).

Table 1. UAV image information.

Flight Date in 2023	28 March and 6 April	3 May	12 June
Image Overlap Rate	75%	75%	75%
Number of Images	1802	1918	1687
Flight Altitude (m)	100	100	100
Image Resolution (cm/pix)	5.87	5.94	5.87
Spatial Coverage (km^2)	1.6	1.74	1.73

2.3. Research Process

The research process involved a detailed analysis of historical flood data from the past five years in the middle and lower reaches of the Wu River basin (Figure 3). This analysis was conducted to identify high-risk, flood-prone zones for targeted UAV aerial reconnaissance. Subsequently, a comprehensive dataset was utilized to construct the HEC-HMS model. This dataset included a 20 m resolution DEM, rainfall and flow data from before and after typhoons and heavy rainfall events, soil classification maps, LULC data, and river cross-section data spanning from 2015 to 2020. Furthermore, aerial images of high-risk, flood-prone areas captured by UAVs were processed using Agisoft Metashape (version 1.4.2, Agisoft LLC: St. Petersburg, Russia) based on the overlapping of UAV images to generate DSMs with resolutions of 10 m, 5 m, and 2 m. Flood simulations were conducted using iRIC, comparing the 20 m resolution DEM provided by LDA with the 10 m, 5 m, and 2 m resolution DSMs derived from UAV images. This comparison aimed to evaluate the accuracy in determining the extent and depth of the flood. Finally, flood scenarios for recurrence intervals of 10, 25, 50, and 100 years were simulated to assess the flood sensitivity of the area.

2.4. HEC-HMS Model

In this study, the research utilized the HEC-HMS 4.10 rainfall–runoff model for hydrological simulations. Originally developed by the U.S. Army Corps of Engineers in 1992, HEC-HMS is a widely recognized tool for simulating runoff in complex watershed systems. It is suitable for both short-term events and long-term observations [17]. Hourly rainfall data were employed as the primary input.

The Wu River basin, covering an area of 561.53 km^2, encompasses 34 sub-watersheds, 19 channels, and 19 confluence points. In the model, the Soil Conservation Service Curve Number method (SCS-CN) was used to estimate rainfall loss. The Soil Conservation Service Unit Hydrograph method (SCS-UH) was utilized to calculate lag time, the Recession method determined baseflow parameters, and the Muskingum–Cunge method was employed for channel parameterization.

To calculate the Soil Conservation Service Curve Number (SCS-CN) parameters, values for imperviousness and curve number (CN) were determined based on the Soil Conservation Service's land use/land cover (LULC) classification system. The average imperviousness for the LULC types within the study area was estimated to be 50%. Additionally, the Soil Conservation Service Unit Hydrograph method (SCS-UH) necessitated calculating the lag time (T_{lag}) for rainfall runoff. For this, an empirical formula specific to the Wu River basin, provided by the Water Resources Agency (WRA), was utilized.

$$T_{lag} = 0.377(L \times L_{ca}/s^{0.5})^{0.257} \tag{1}$$

where T_{lag} = lag time (h), L = longest flowpath length, L_{ca} = centroidal flowpath length, and s = basin slope. The parameters required for the recession method include initial discharge, recession constant, and ratio to peak. The Muskingum–Cunge method requires parameters such as channel length, channel slope, channel width, and Manning's coefficient. All parameter settings in the HEC-HMS model are listed in Table 2.

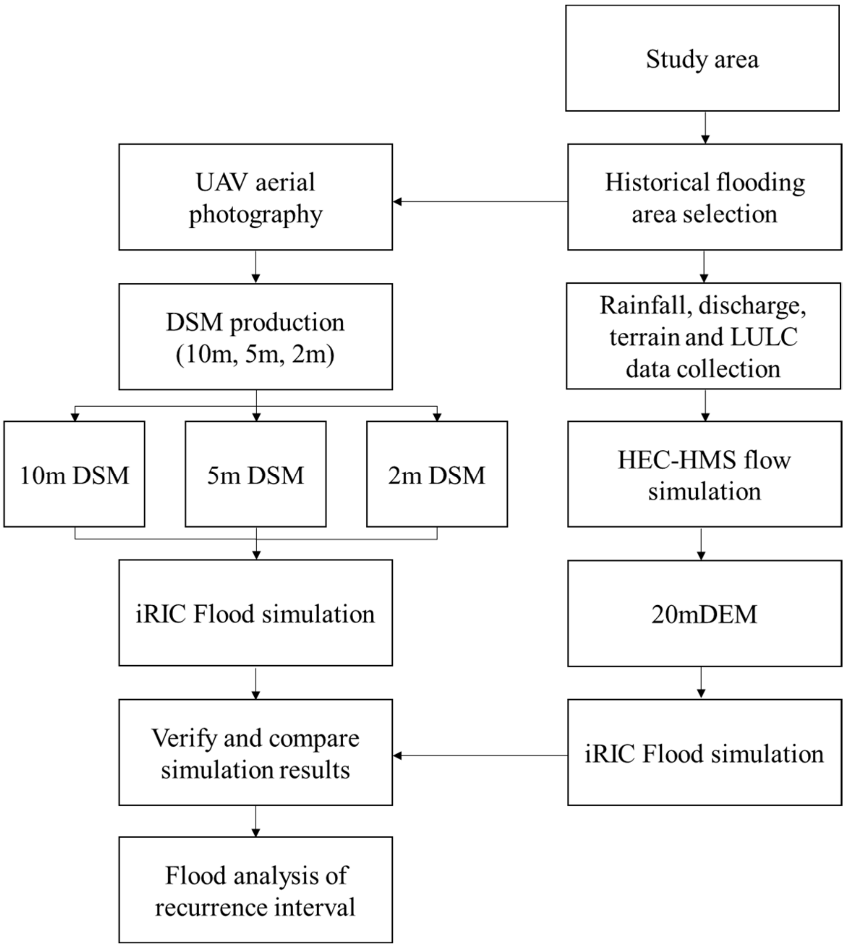

Figure 3. Research flowchart.

Table 2. HEC-HMS parameter settings.

Parameter	Method	Unit	Value (Min/Max)
Curve Number	SCS-CN	dimensionless	62.87/79.16
Impervious		%	50
Lag Time	SCS-UH	min	52.25/154.76
Initial Discharge	Recession	cm	3
Recession Constant		dimensionless	0.95
Ratio to Peak		dimensionless	0.01
Channel Length	Muskingum–Cunge	m	810.0/9310.1
Channel Slope		m	38.8/693.7
Channel Width		m/m	0.0/0.02
Manning's Coefficient		dimensionless	0.04

Rainfall data from Typhoon Saola in 2012 and Typhoon Soulik in 2013 were used for model calibration, while the heavy rainfall event on 20 May 2019 was utilized for model validation. The observed data from the Chi-Nan Bridge flow station were crucial in both the calibration and validation processes. To assess the performance of the hydrological model, this study relied on two widely recognized indicators: Nash–Sutcliffe efficiency (*NSE*) and percentage error in peak flow (*PEPF*). These are commonly used in hydrological research [42] and have found extensive application in studies related to the HEC-HMS model, serving as common benchmarks for model development and parameter optimization. The formulas are as follows:

$$NSE = 1 - \frac{\sum_{i=1}^{n} (O_i - S_i)^2}{\sum_{i=1}^{n} (O_i - \overline{O})^2} \tag{2}$$

$$PEPF = \left| \frac{O_i - S_i}{O_i} \right| \times 100\% \tag{3}$$

where n: total observations, O_i = value of ith observation, S_i = value of ith simulation, and O_i = mean of observations.

2.5. IRIC Model

In this study, the Nays2DFlood solver in iRIC 3.0.19 was utilized for flood simulation. This solver is commonly used because it can accommodate flood simulation without detailed bathymetric data from the study rivers. Specifically, Nays2DFlood uses general curvilinear coordinates to model two-dimensional unsteady flow patterns, effectively accommodating both river channels and floodplains within its coordinate system. Notably, it is capable of simulating diverse flow conditions, whether from upstream or side rivers, as required [23].

A key advantage of this solver is its minimal data requirements. It requires only DEM, rainfall data, and flow data, thus eliminating the need for detailed river channel information. This feature makes it especially useful for analyzing flood processes in undeveloped rivers and river systems in developing regions, where comprehensive data might not be readily available [25].

Nays2DFlood calculates the continuity and motion equations for a rectangular two-dimensional unsteady flow field, which are represented by the following equations [43].

$$\frac{\partial h}{\partial t} + \frac{\partial (hu)}{\partial x} + \frac{\partial (hv)}{\partial y} = q + r, \tag{4}$$

$$\frac{\partial (hu)}{\partial t} + \frac{\partial (hu^2)}{\partial x} + \frac{\partial (huv)}{\partial y} = -hg\frac{\partial H}{\partial X} - \frac{\tau_x}{\rho} + D^x, \tag{5}$$

where

$$\frac{\tau_x}{\rho} = C_f u \sqrt{u^2 + v^2} \tag{6}$$

$$\frac{\tau_x}{\rho} = C_f v \sqrt{u^2 + v^2}, \tag{7}$$

$$D^x = \frac{\partial}{\partial x}\left[v_t \frac{\partial (hu)}{\partial x}\right] + \frac{\partial}{\partial y}\left[v_t \frac{\partial (hu)}{\partial y}\right] \tag{8}$$

$$D^y = \frac{\partial}{\partial x}\left[v_t \frac{\partial (hv)}{\partial x}\right] + \frac{\partial}{\partial y}\left[v_t \frac{\partial (hv)}{\partial y}\right] \tag{9}$$

where h = water depth, t = time, u = flow velocity in x direction, v = flow velocity in y direction, g = gravitational acceleration, H = water surface elevation, r = rainfall, τx = riverbed shear stress in x direction, τy = riverbed shear stress in y direction, Cf = riverbed friction coefficient, vt = eddy viscosity coefficient, ρ = density of water, q = inflow through a box culvert.

The construction of the iRIC model comprises three key aspects: calculation conditions, object settings, and boundary conditions. Prior to configuring each of these components, various data sources are integrated into the model. This includes importing a 20 m resolution DEM provided by LDA and DSMs with resolutions of 10 m, 5 m, and 2 m captured via UAVs to establish the topographic data. Additionally, imagery obtained from Sentinel-1 is incorporated as the background.

Calculation conditions follow default parameters, utilizing the upwind method for finite difference equation calculations. The input parameters include rainfall data and time intervals. Rainfall data from the 20 May to 21 May 2019 series are weighted using the Thiessen polygon method. The time interval is set at 0.01 s to satisfy the Courant–Friedrichs–Lewy (CFL) condition, thereby optimizing the model's computational efficiency.

Object settings commence with the definition of the simulation area and grid sizes. The iRIC model covers an area of approximately 1.05 km^2, and grid sizes are set at 20 m, 10 m, 5 m, and 2 m resolutions, each corresponding to the respective DEM and DSM. A surface roughness value of 0.055 is assigned following the equation of [43]. Impermeable structures such as river embankments, road embankments, and the extents of buildings are outlined using orthophotos obtained from UAV imagery and Sentinel-1 data. Boundary conditions require specifying the river slope and flow data. For this simulation, in an area with a flat river channel, the slope is set at 0.001. The flow data are derived from the HEC-HMS simulation results conducted between May 20th and 21st, 2019.

2.6. UAV-DSM and Orthophoto

Orthophotos and DSMs were generated using Agisoft Metashape, an image processing software. The process began with importing and aligning images captured during UAV flight missions. To ensure precision, a network of 26 ground control points (GCPs) and 14 check points (CPs) was strategically established across the flight area for even distribution within the flyable region (Figure 4). In general, GCPs calibrate UAV images during the mapping process, while CPs verify the accuracy of the mapped area. Of these 40 points, 21 were located on the left bank and 19 on the right bank.

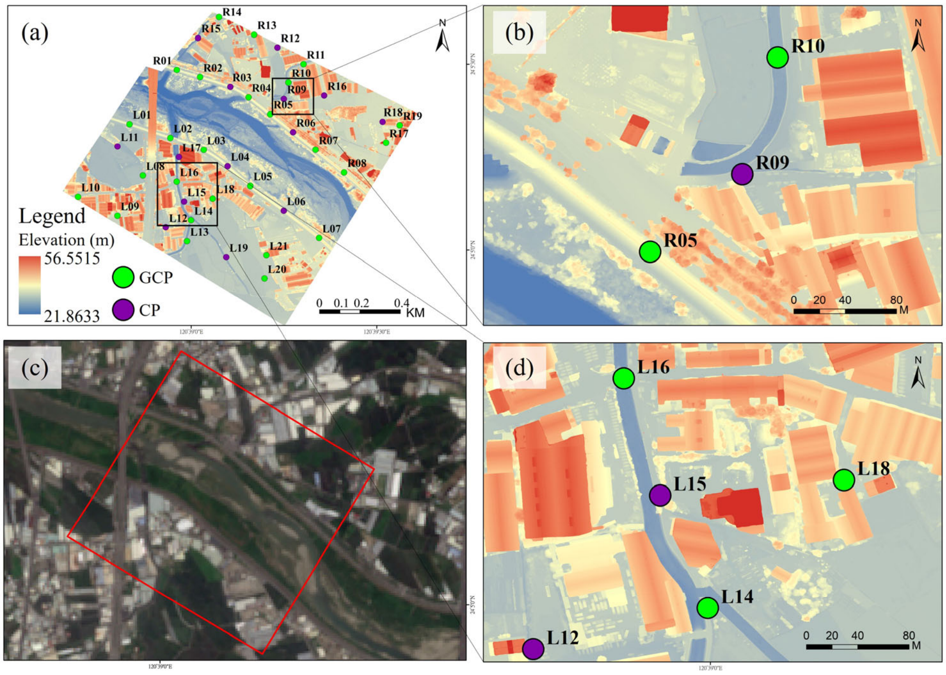

Figure 4. Distribution map of ground control points and check points in subfigure (**a**), and subfigure (**c**) shows the satellite image derived from Sentinel-2 of 23 March 2023. The study area is highlighted with a red box. Partial enlarged DSMs in subfigures (**b**,**d**).

The coordinates of these GCPs were precisely measured using the Trimble R12 RTK mobile station and a virtual survey station (e-GNSS) set up by the National Land Surveying and Mapping Center. Following this, aerial triangulation adjustments were performed, integrating three-dimensional spatial coordinates. This crucial step established the spatial relationship between the images and the GCPs, thus enabling the derivation of three-dimensional spatial coordinates for the entire flight area. Consequently, this process led to the generation of both orthophotos and DSMs (Figure 5).

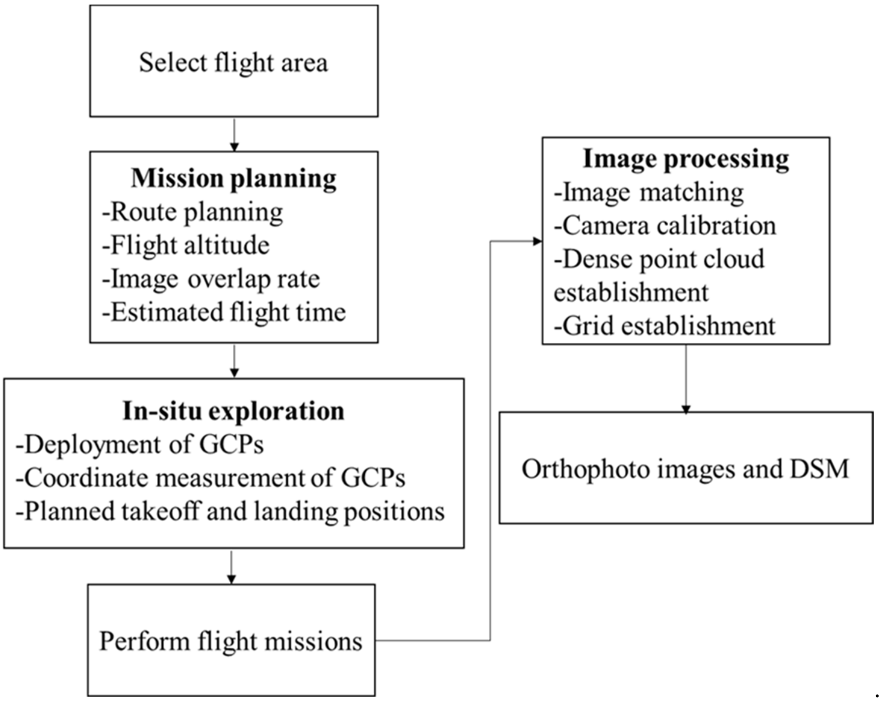

Figure 5. Orthophoto and DSM construction flowchart.

3. Results

This section may be divided by subheadings. It should provide a concise and precise description of the experimental results, their interpretation, as well as the experimental conclusions that can be drawn.

3.1. Calibration and Validation of HEC-HMS Model

In the analysis of flood events, examining the variation in peak flow is crucial, as its accuracy significantly impacts the model's quality. The flow time series and analysis results for Typhoon Saola (2012), Typhoon Soulik (2013), and the heavy rainfall event on 20 May 2019 are illustrated in Figure 6a–c. Detailed simulation outcomes are provided in Table 3. The simulations for Typhoon Saola (2012) and the 20 May 2019 rainfall event predicted flows slightly lower than the observed data, while the simulation for Typhoon Soulik (2013) predicted a flow marginally higher than the actual data. In terms of *NSE*, the simulation for Typhoon Saola (2012) achieved the highest accuracy. Conversely, the simulation for Typhoon Soulik (2013) excelled in the *PEPF*, with the 20 May 2019 event ranking second in both metrics.

Table 3. Evaluation of simulation results for calibration and validation.

	Calibration		**Validation**
	Typhoon Saola in 2012	**Typhoon Soulik in 2013**	**Heavy Rainfall on 20 May 2019**
Simulated Discharge (cm)	3791.2	3262.5	2856.8
Observed Discharge (cm)	3988.7	3206.4	2951.2

Table 3. *Cont.*

	Calibration		Validation
	Typhoon Saola in 2012	**Typhoon Soulik in 2013**	**Heavy Rainfall on 20 May 2019**
NSE	0.93	0.88	0.9
PEPF (%)	4.94	1.75	3.2

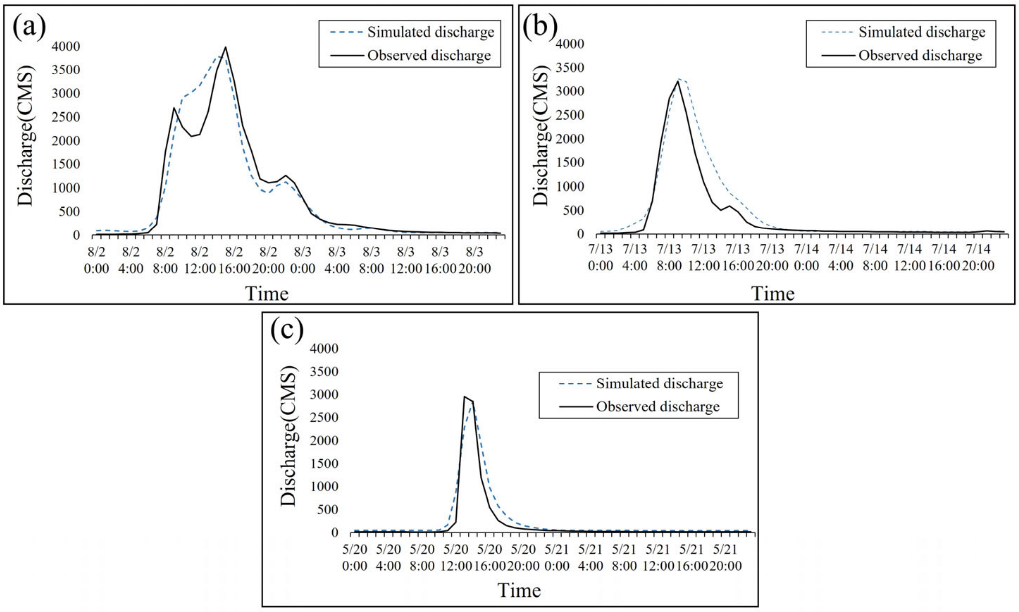

Figure 6. HEC-HMS flow simulation results for each rainfall event: (**a**) Typhoon Saola in 2012, (**b**) Typhoon Soulik in 2013, (**c**) heavy rainfall on 20 May 2019.

3.2. UAV-DSM Accuracy Assessment

The results of the monthly DSM construction were evaluated using the root mean square error (RMSE) as the metric. Figure 2 illustrates the DSM and the orthophoto. Table 4 presents the errors for ground control points and check points from April to June, with the minimum error values for each month highlighted in bold. On 28 March and 6 April, the error for ground control points was 2.12 cm, and the error for check points was 6.37 cm. The highest error for ground control points occurred on 3 May at 4.10 cm, accompanied by a check point error of 8.82 cm. On 12 June, the error for ground control points reduced to 3.182 cm, and the check point error was 6.44 cm. Notably, the smallest elevation error (Z-direction) for the check points was 3.14 cm.

Table 4. Differences in ground control points (26 points) and check points (14 points) for each month.

Type	Flight Date	RMSEX (cm)	RMSEY (cm)	RMSEZ (cm)	RMSEXYZ (cm)
GCP	28 March and 6 April	**1.62**	**1.25**	0.54	**2.12**
	5/3	2.96	2.77	0.59	4.10
	6/12	2.12	2.31	**0.53**	3.18
	Average	2.24	2.11	0.55	3.13
CP	28 March and 6 April	**3.26**	**3.91**	3.83	**6.37**
	3 May	5.21	6.22	3.46	8.82
	12 June	3.65	4.27	**3.14**	6.44
	Average	4.04	4.80	3.47	7.21

Note: RMSEX: the RMSE in the x-axis direction; RMSEY: the RMSE in the y-axis direction; RMSEZ: the RMSE in the z-axis direction; RMSEXYZ: the RMSE in the all-axis direction. The minimum differences are highlighted in bold.

3.3. IRIC Model Simulations

According to the disaster survey report from the NCDR, the heavy rainfall on 20 May 2019 resulted in significant flooding in the downstream areas of the Wu River, especially in the Wuri and Wufeng Districts of Taichung City. Notable instances of flooding with specific locations and depths were recorded in Wuguang and Wufu Villages (Table 5). It is important to note that flooding point A was reported without a corresponding flood depth measurement. In this research, the Ministry of the Interior's 20 m resolution DEM and UAV-generated DSMs at 10 m, 5 m, and 2 m resolutions were employed for iRIC flood simulation. This involved comparing the flood simulation results from the DEM and DSMs of varying resolutions with the actual flood depths recorded during the event. The simulated area covered approximately 1.05 km^2, and the RMSE was calculated to evaluate the accuracy of the simulation. The results of the flood simulation using both DEM and DSM are presented in the subsequent subsections.

Table 5. Information on flood locations on 20 May 2019.

Flood Point	Report Agency	Flood Depth (m)
A	Citizen report	-
B	EMIC	0.6
C	EMIC	1
D	EMIC	0.5
E	Third River Management Office	0.7
F	EMIC	0.7
G	EMIC	0.5

Note: EMIC: Emergency Management Information System.

3.3.1. 20 m DEM Simulation Results

The flood simulation using a 20 m resolution DEM showed that the smallest negative error (the difference between simulation and observation) was −0.045 m at point B, suggesting a minor underestimation (Figure 7 and Table 6). The largest underestimation was observed at point E, with a more substantial error of −0.556 m. The overall RMSE for these simulation results was calculated to be 0.370 m.

Table 6. Flood depth simulation results of 20 m resolution DEM.

Flood Point	Flood Depth (m)	Simulation Depth (m)	Difference (m)	RMSE (m)
A	-	0.62	-	0.37
B	0.6	0.56	−0.05	
C	1	0.5	−0.5	
D	0.5	0.28	−0.23	
E	0.7	0.14	−0.56	
F	0.7	0.26	−0.45	
G	0.5	0.6	0.1	

3.3.2. 10 m, 5 m, and 2 m DSM Simulation Results

Flood simulations using a 10 m resolution DSM for the period between April and June showed that the simulation estimated flood depth using the elevation of the nearest road surface for flood points situated on buildings (Figure 8 and Table 7). The results showed a notable discrepancy at flood point C, while the simulated depth at flood point E was zero. Although the error at flood point A could not be precisely measured, the observed flood depth there exceeded 3 m. The flood simulations using a 5 m resolution DSM revealed larger errors at flood points C and E, while demonstrating smaller errors at points D and F (Figure 9 and Table 8). The most accurate simulation was conducted on 3 May, yielding a RMSE of 0.293 m. The iRIC flood simulation utilizing a 2 m resolution

DSM showed that the smallest error values for each column and row are emphasized in bold (Figure 10 and Table 9). Notably, the simulation errors at flood points B and C were significantly large. Apart from flood point F, the simulation results along the right bank of the river demonstrated high accuracy, with the best performance recorded on 12 June, indicated by an RMSE of 0.243 m. Generally, most of the simulation depth was smaller than the flood depth (Tables 7–9), and the average RMSE values were smaller in bold, while the resolution of DSM were finer. These discrepancies are likely attributable to the DSM's limited resolution, which may not accurately reflect the elevation variations in the surface features.

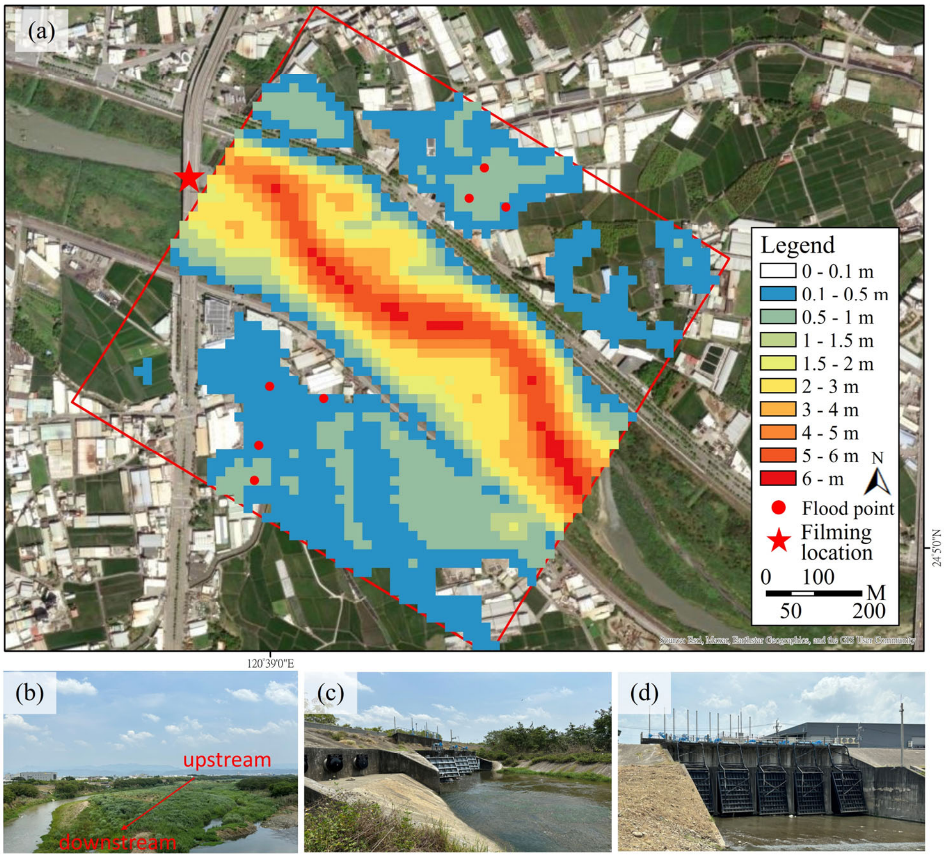

Figure 7. Simulation results of 20 m resolution DEM in (**a**), with in situ photos of river and drainage facilities in (**b**–**d**).

Table 7. Flood depth simulation results of 10 m resolution DSM.

Flood Point	**Flood Depth (m)**	**28 March and 6 April**		**3 May**		**12 June**	
		Simulation Depth (m)	**Difference (m)**	**Simulation Depth (m)**	**Difference (m)**	**Simulation Depth (m)**	**Difference (m)**
A	-	4.23	-	3.09	-	6.09	-
B	0.6	0.71	0.11	1.13	0.53	2.06	1.46
C	1	0.24	−0.76	0	−1	0.47	−0.54
D	0.5	0.24	−0.27	0.2	−0.3	0.1	−0.4
E	0.7	0	−0.7	0	−0.7	0	−0.7
F	0.7	0.49	−0.21	0.44	−0.26	0.59	−0.11
G	0.5	0.21	−0.29	0.33	−0.17	0.21	−0.29
RMSE		**0.462**		0.571		0.725	

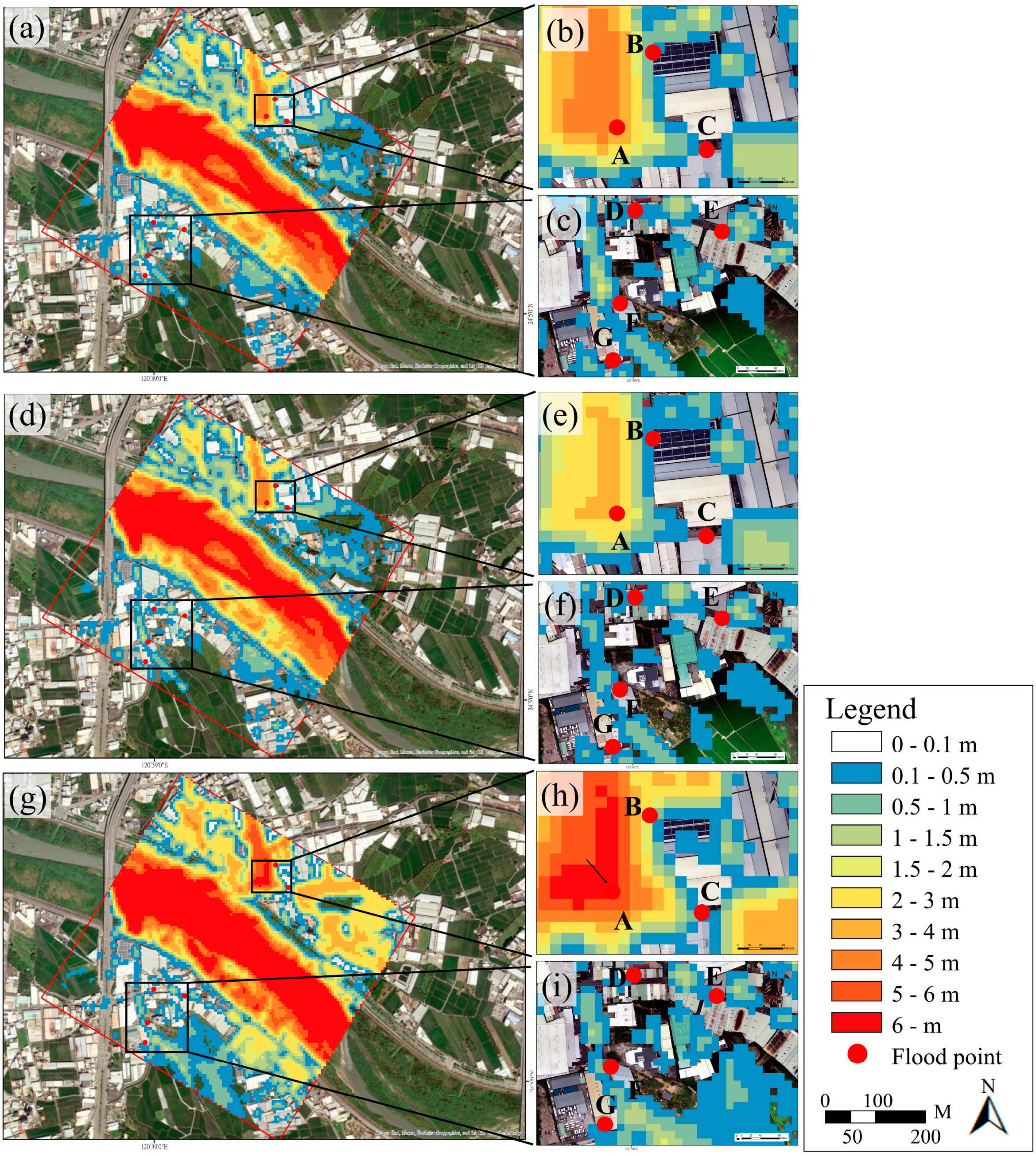

Figure 8. 10 m resolution DSM simulation results are shown for April, May, and June in subfigures (**a**–**c**), (**d**–**f**), (**g**–**i**), respectively. The study area is highlighted in a red box and two enlarged area are marked by black boxes.

Table 8. Flood depth simulation results for 5 m resolution DSM.

Flood Point	Flood Depth (m)	28 March and 6 April		3 May		12 June	
		Simulation Depth (m)	Difference (m)	Simulation Depth (m)	Difference (m)	Simulation Depth (m)	Difference (m)
A	-	0.46	-	0.39	-	0.32	-
B	0.6	0.36	−0.24	0.37	−0.23	0.49	−0.12
C	1	0.49	−0.51	0.54	−0.46	0.28	−0.72
D	0.5	0.62	0.12	0.46	−0.04	0.32	−0.18
E	0.7	0.16	−0.54	0.22	−0.48	0.3	−0.4
F	0.7	0.53	−0.17	0.58	−0.12	0.62	−0.08
G	0.5	0.15	−0.36	0.54	0.04	0.2	−0.3
RMSE		0.361		**0.293**		0.372	

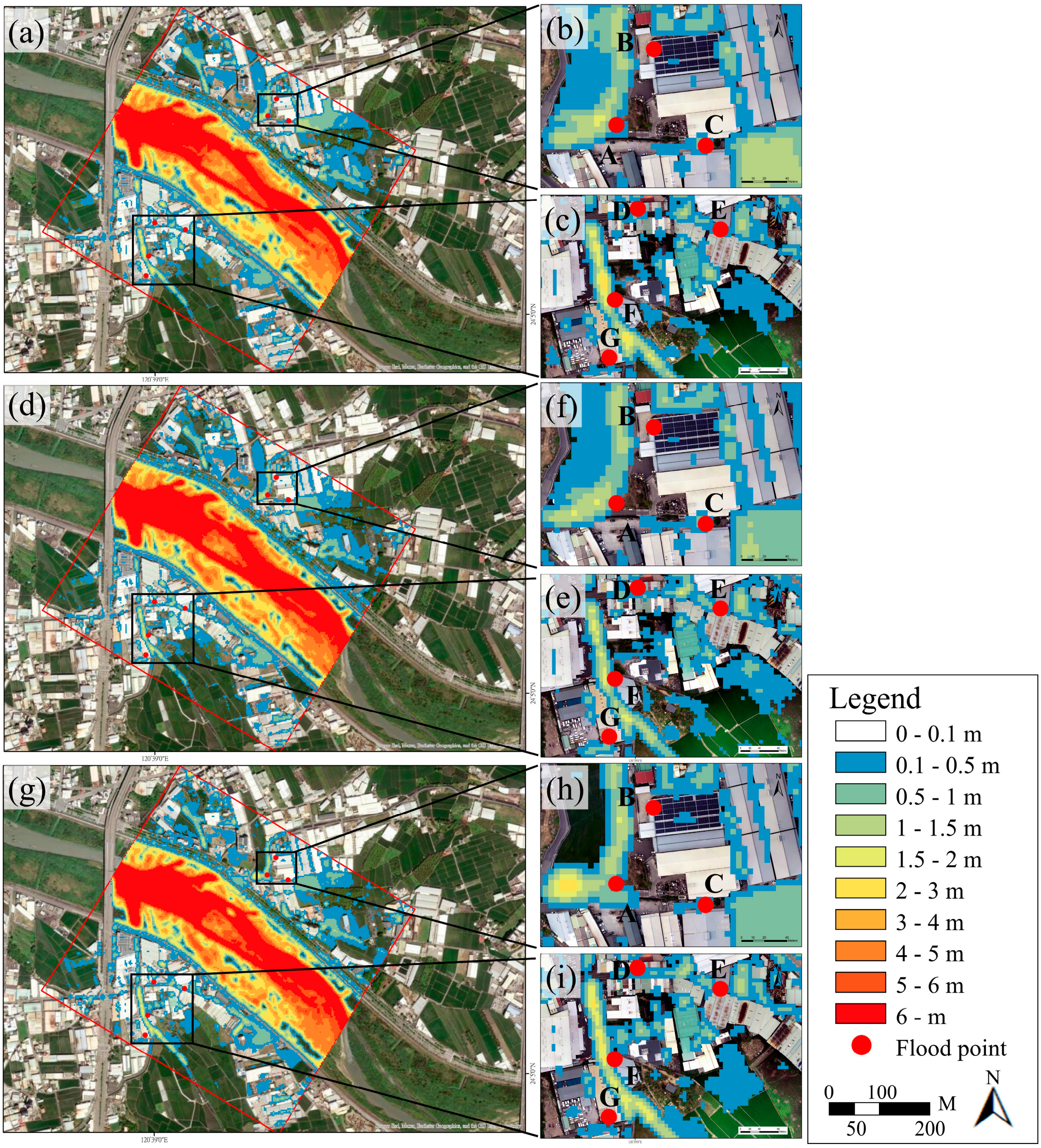

Figure 9. 5 m resolution DSM simulation results are shown for April, May, and June in subfigures (**a**–**c**), (**d**–**f**), (**g**–**i**), respectively. The study area is highlighted in a red box and two enlarged area are marked by black boxes.

Table 9. Resolution 2 m DSM flood depth simulation results.

Flood Point	Flood Depth (m)	28 March and 6 April		3 May		12 June	
		Simulation Depth (m)	Difference (m)	Simulation Depth (m)	Difference (m)	Simulation Depth (m)	Difference (m)
A	-	0.27	-	0.24	-	0.26	-
B	0.6	0.15	−0.45	0.15	−0.45	0.23	−0.37
C	1	0.53	−0.47	0.6	−0.4	0.64	−0.36
D	0.5	0.45	−0.04	0.5	−0.01	0.45	−0.05
E	0.7	0.73	0.03	0.78	0.08	0.81	0.11
F	0.7	0.42	−0.28	0.36	−0.34	0.44	−0.26
G	0.5	0.47	−0.03	0.4	−0.1	0.41	−0.09
RMSE		0.291		0.286		**0.243**	

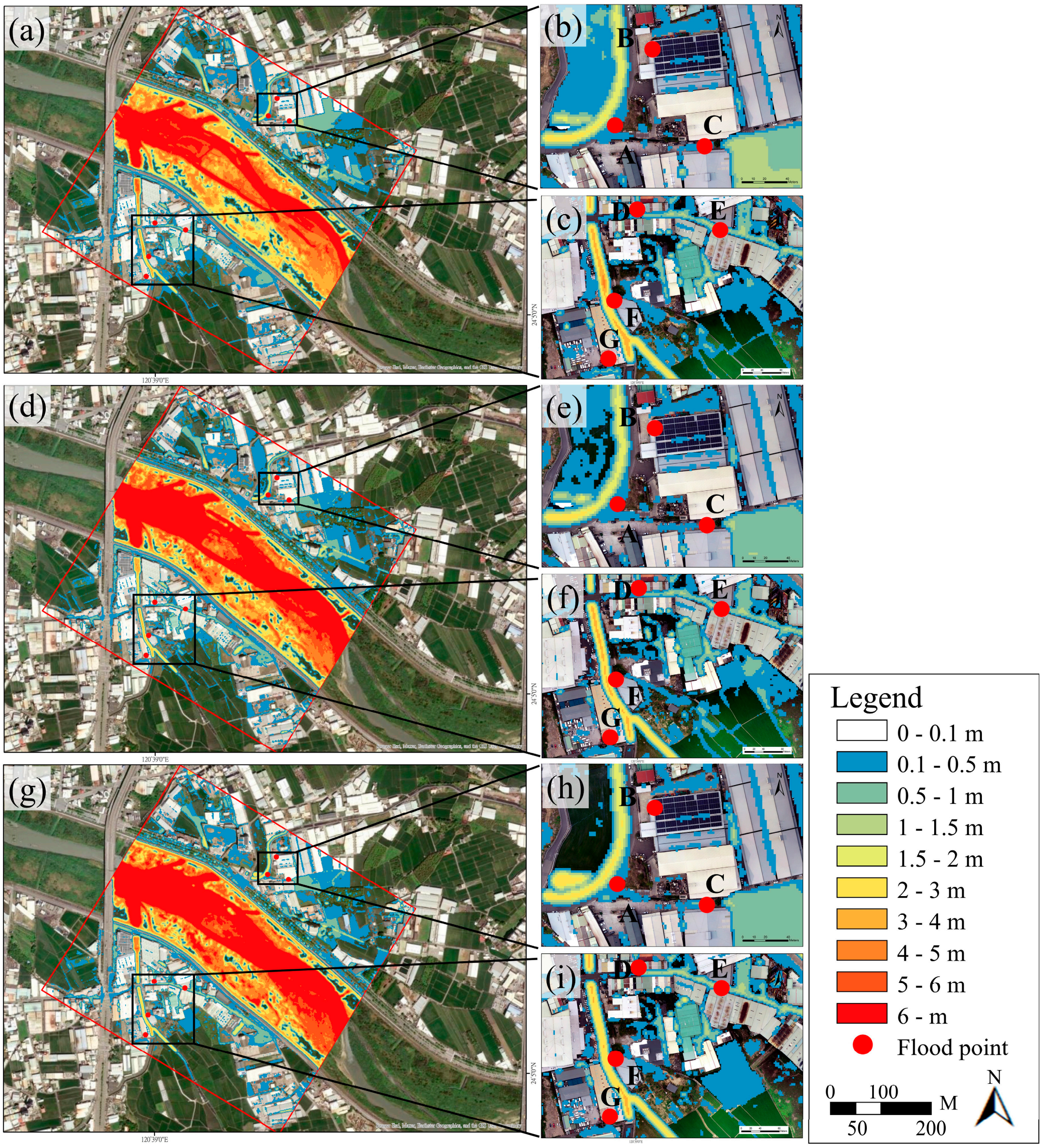

Figure 10. 2 m resolution DSM simulation results are shown for April, May, and June in subfigures (**a**–**c**), (**d**–**f**), (**g**–**i**), respectively. The study area is highlighted in a red box and two enlarged area are marked by black boxes.

3.4. Flood Simulation and Recurrence Intervals

3.4.1. Flood Simulation for Different Recurrence Intervals

As detailed in Section 3.3, the simulation results originated from a single short-duration heavy rainfall event. However, the flood prevention infrastructure in the Wu River basin is generally engineered to endure rainfall events with a 100-year recurrence interval. To evaluate the robustness of these structures in the face of evolving rainfall patterns, multiple flood scenarios at different recurrence intervals within the simulation area were analyzed.

Utilizing the optimal flood simulation with a 2 m resolution DSM, parameters were maintained consistently while simulating various recurrence intervals (Figure 11 and Table 10). The simulations revealed no riverine flooding at any interval; however, flooding began on the left and right riverbanks after 10 and 25 years, respectively. Flooding points A, C, D, and E, characterized by their low elevation and drainage issues, exhibited significant flooding at the 10-year interval, underscoring their susceptibility in the study area. Points D and E showed minimal variation in flood depth across intervals. In contrast, the flood depth at point C remained relatively unchanged at the 10-year and 25-year intervals. However, at the 50-year and 100-year intervals, the flood depth at point C increased dramatically, likely due to the topography of the area and the flooding of nearby roads at these higher intervals, resulting in greater water accumulation at this point.

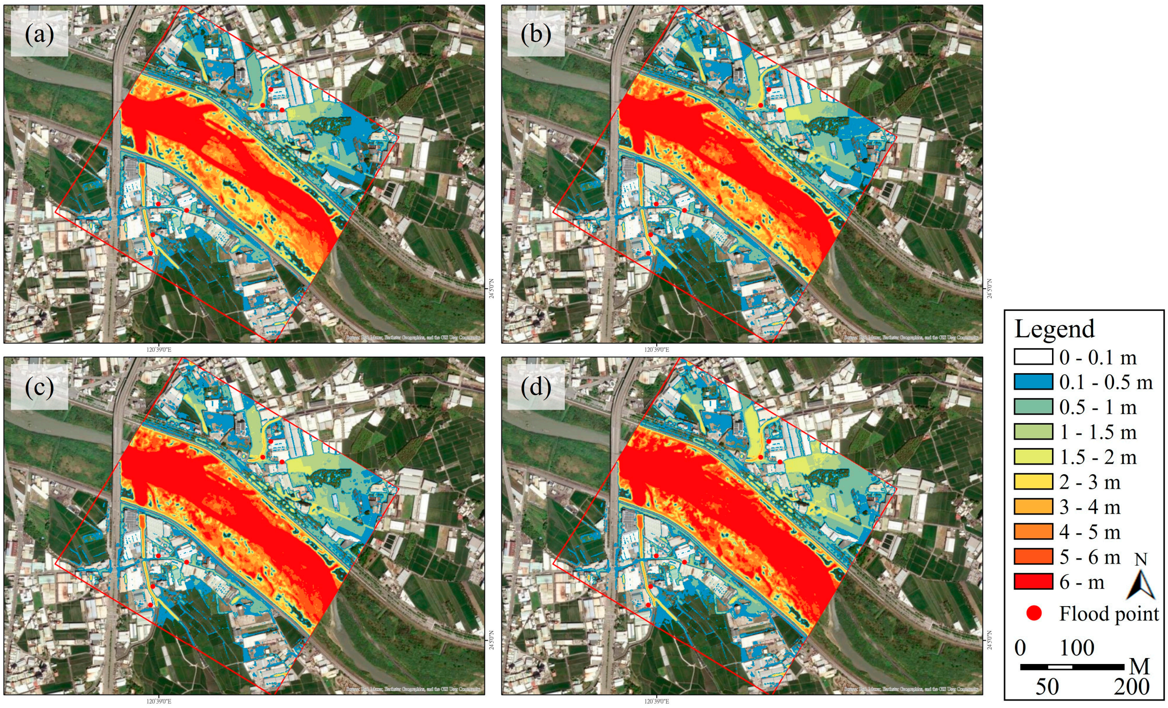

Figure 11. Simulation results for 10-year, 25-year, and 100-year recurrence intervals are shown in subfigure (**a**), (**b**), and (**c**), (**d**), respectively. The study area is highlighted in a red box.

Table 10. Flood depth and range at each flooding point for different recurrence intervals.

	Recurrence Intervals Food Depth (m)			
Flood Point	**10-Year**	**25-Year**	**50-Year**	**100-Year**
A	0.94	1.28	1.5	1.7
B	0.21	0.45	0.62	0.81
C	0.6	0.62	0.83	1.02
D	0.4	0.43	0.44	0.46
E	0.81	0.86	0.89	0.95
F	0.23	0.29	0.38	0.42
G	0.23	0.37	0.43	0.47

3.4.2. Flood Analysis for Recurrence Intervals

Utilizing Taiwan’s existing third-generation potential inundation maps https://data.gov.tw/dataset/25766 (assessed on 1 September 2022), the simulation scenarios for 350 mm and 650 mm of rainfall within 24 h were aligned with the rainfall amounts for the 10-year (368.2 mm) and 100-year (614.0 mm) recurrence intervals, respectively. These scenarios were therefore selected for comparative analysis. In these simulations, local agricultural land, designated as a flood detention area, and built-up land were excluded from the inundation calculations, in line with the use of DSM in recurrence interval flood simulations. Analysis of the areas for each recurrence interval, potential inundation areas, and their intersections (as shown in Figure 12 and Table 11) revealed that the simulation for the 10-year recurrence interval encompassed a larger area than the potential inundation for a 350 mm rainfall event in 24 h, with an overlap rate of 24.1%. In the case of the 100-year interval, the simulation's overlap with the potential inundation area for a 650 mm rainfall event in 24 h was significantly higher, at 41.0%.

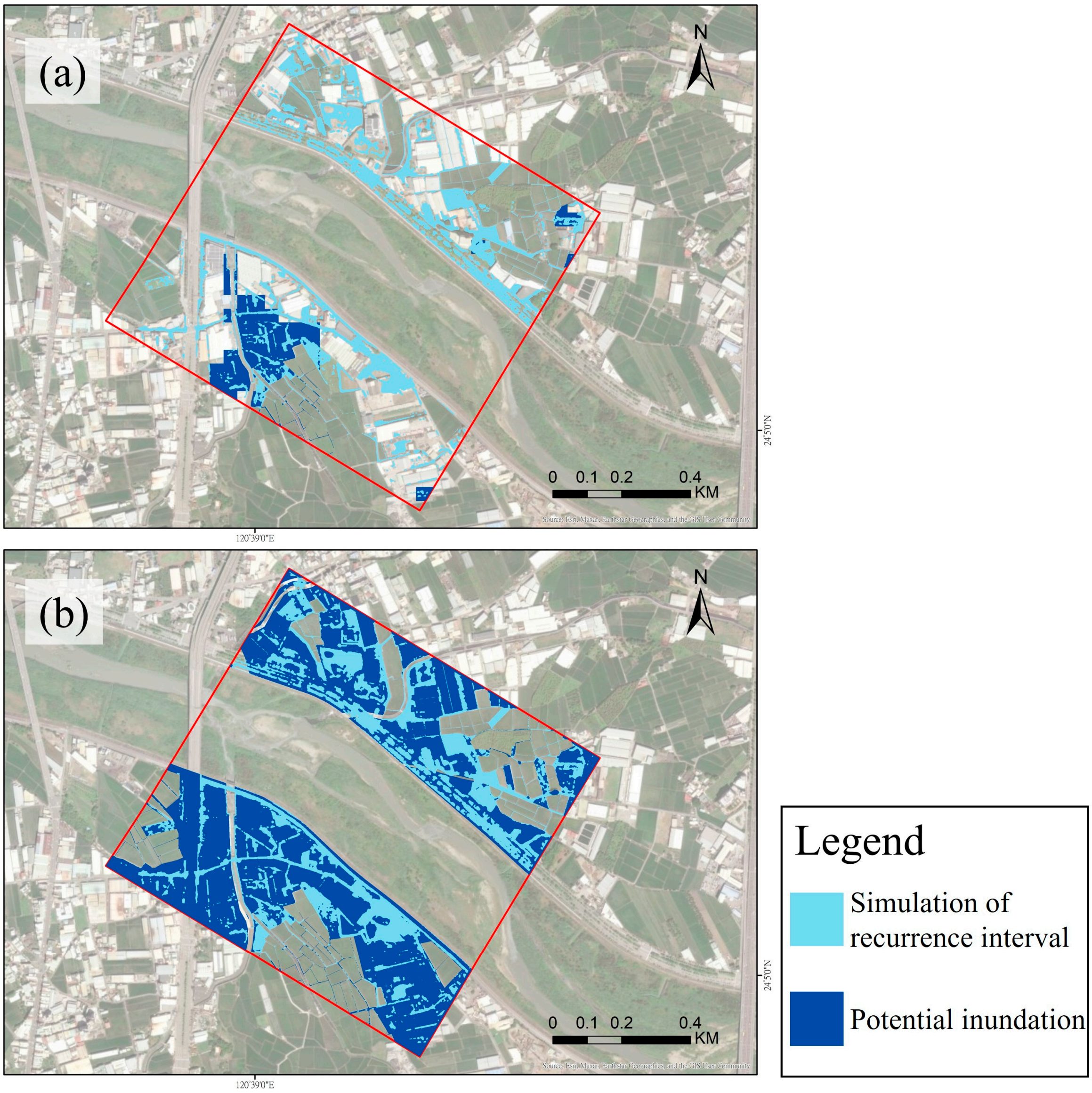

Figure 12. (**a**) The flood simulation range for a 10-year recurrence interval and 24 h 350 mm rainfall. (**b**) The flood simulation range for a 100-year recurrence interval and 24 h 650 mm rainfall. The study area is highlighted in a red box.

Table 11. The flood simulation and potential inundation area for each recurrence interval.

Flood Area of Recurrence Interval (m^2)		**Flood Area of Potential Inundation (m^2)**		**Overlap Area (m^2)**	**Overlap Rate (%)**
10 (year)	151,980.2	24 h 350 mm	37,461.1	9031.6	24.1
100 (year)	184,575.7	24 h 650 mm	271,121.4	111,172.6	41

4. Discussion

In this study, HEC-HMS was utilized for flow simulation, incorporating DEM and UAV imagery with 20 m resolution to create DSMs at 10 m, 5 m, and 2 m resolutions for iRIC flood range and depth simulations. The research focused on analyzing the similarities and differences in the simulation results across various months and resolutions. Furthermore, it involved calculating rainfall amounts for different recurrence intervals to simulate flow and examine flooding patterns at each point under diverse conditions.

4.1. Applicability of the HEC-HMS Model

Based on the HEC-HMS simulation results presented in Section 3.1, the model achieved *NSE* greater than 0.88 and *PEPF* of less than 5% for three flood events. These outcomes were compared with those of related studies to assess the suitability of the HEC-HMS model for the Wu River basin. For instance, Ref. [44] used the HEC-HMS model for hydrological simulations in Ethiopia's Gilgel Abay watershed, covering nine rainfall events. They dedicated six events to parameter calibration and optimization and the remaining three to validation, achieving an *NSE* of 0.884 and a *PEPF* of 1.49%. Similarly, Ref. [18] conducted simulations for twelve flood events in the Chuanchang River basin, Fujian, China, using nine events for establishing model parameters and three for validation, resulting in an *NSE* of 0.81 and a *PEPF* of less than 15% for each event. In our research, the calibration and validation of the simulation results yielded an *NSE* greater than 0.884 and a *PEPF* of less than 4.94%, exceeding the optimal standards set by [42]. These results are comparable to those of the aforementioned studies, confirming the effectiveness of the HEC-HMS model for rainfall–runoff simulations in the middle and lower reaches of the Wu River basin.

4.2. Effectiveness of Using UAV-DSM

On 3 May, some images showed overexposed blank points, which complicated the identification of their centers. As a result, the DSM constructed for that month exhibited the largest error. Ref. [45] used UAVs for photographic surveys in urban parkland in Glasgow, Scotland, and conducted an error analysis on the layout of control points. They suggested that placing a GCP approximately every 2 hectares could reduce the xy-axis error to 0.076 m and the z-axis elevation error to 0.08 m. They also noted that increasing the density of control points does not necessarily lead to a significant reduction in error. In this research, except for the larger xy-axis error observed in the check points on 3 May, the results from the other two data collection efforts were superior to those reported by Coveney and Roberts. Stott et al. (2020) collected data along a 2 km stretch of a braided river in Glen Feshie, UK, using a DJI Phantom 4 RTK for topographic mapping. Their RMSE values for check points were 0.023 m on the y-axis and 0.072 m on the z-axis. Although the RMSE for the check points in the y-axis in this study was higher than that reported by Stott et al., the z-axis RMSE was lower. This comparison demonstrates the effectiveness of UAVs for riverine mapping, and the topographic mapping conducted in this research is consistent with related literature, confirming its practicality.

4.3. Improvement of iRIC Model Simulation by Using UAV-DSM

In this research, we utilized the flood depth measurements at various points to verify the accuracy of the iRIC simulations. This approach provides an alternative method for confirming the reliability of the iRIC model in flood simulations. In a similar vein, Ref. [9] integrated simulation results from HEC-HMS and iRIC. They validated the iRIC simulation results using flood range data from the Department of Irrigation in Sri Lanka and employed these findings to develop local flood risk maps.

The analysis of iRIC simulations at varying resolutions showed that, with the 20 m DEM, the river's left bank was prone to overflow. In contrast, the 10 m DSM simulations for each month indicated a potential overflow on the right bank. However, water level data from the Chi-Nan Bridge on 20 May 2019 revealed no actual overflow on that date. This discrepancy suggests that lower-resolution elevation data might not accurately capture the topographical nuances between the embankment and the river channel, leading to simulated flood extents that diverge from actual conditions. On the other hand, simulations using 5 m and 2 m DSM resolutions did not indicate overflow, and the flood extents accurately followed the road and drainage systems. This demonstrates that the 5 m and 2 m DSM resolutions are sufficiently detailed to capture elevation differences between objects, thus providing a more accurate representation of the actual flood situation. Notably, the smallest flood depth errors at most points (except for points B and F) were observed with the 2 m DSM resolution.

In addition, the iRIC model, when utilizing DSM, demonstrated improved simulation accuracy for the left bank (at flood points D, E, F, G) compared to the right bank (at flood points B, C). The heavy rainfall event on 20 May 2019 caused some damage to the embankments. Subsequent repairs and heightening of these embankments resulted in increased simulation errors for flood depth on the right bank. Therefore, the overall simulation accuracy, represented by the RMSE for the entire area (RMSEA), was compared with the simulation accuracy for the left bank (RMSEL) (Table 12). The RMSE values for the left bank (at flood points D, E, F, G) showed a decrease in each resolution's simulations. The 10 m and 5 m resolution simulations were most accurate in May, with RMSEs of 0.411 m and 0.248 m, respectively, while the 2 m resolution simulations achieved the highest accuracy in April, with an RMSE of 0.143 m.

Table 12. Comparison of overall simulation results and left bank simulation results for each resolution of DEM and DSM.

	28 March and 6 April		**3 May**		**12 June**	
Resolution	**RMSEA**	**RMSEL**	**RMSEA**	**RMSEL**	**RMSEA**	**RMSEL**
10 m	0.46	0.42	0.57	0.41	0.47	0.43
5 m	0.36	0.34	0.29	0.25	0.37	0.27
2 m	0.29	0.14	0.29	0.18	0.24	0.15

Unit: m. RMSEA stands for the RMSE for the entire area while RMSEL stands for the RMSE for the left bank.

The expected overlap between the iRIC simulation results for each recurrence interval and the existing potential inundation maps is anticipated to be minimal. This discrepancy arises because the potential inundation maps are based on a coarser 40 m × 40 m simulation grid and DEM geographic data, which assume free-flowing conditions without considering the presence of physical objects. Consequently, in built-up areas, these maps may produce simulated flood depths that are more reflective of the surrounding terrain rather than the actual flood conditions, especially where objects are present. In contrast, this study employed a finer 2 m × 2 m grid for simulating floods at various recurrence intervals, utilized DSM geographic data, and incorporated box culvert configurations. This approach allowed the simulation to deliberate the influence of surrounding objects and drainage facilities, enabling the flood extent to more accurately follow roads and represent the real flood conditions around objects. Despite the variations in rainfall patterns and methods for calculating precipitation between the recurrence interval simulations and the potential inundation maps, the latter remains the primary reference for assessing flood risk in the country. Therefore, this study compares the recurrence interval simulation results with the third-generation potential inundation maps, presenting an alternative approach to flood simulation.

5. Conclusions

In this study, the HEC-HMS hydrological model was utilized to simulate flow data, and high-resolution UAV-DSMs were integrated into the iRIC for assessing flood depths at various DSM resolutions. The study demonstrates that the combination of simulated flow data and detailed digital surface models significantly enhances the accuracy of flood depth estimation. When validated against historical heavy rainfall events, the HEC-HMS simulations showed high *NSE* values exceeding 0.88 and *PEPF* below 5%, affirming their reliability for this purpose. In terms of iRIC flood simulations, the most accurate results were obtained using a 2 m resolution UAV-DSM, indicating that higher-resolution DSMs can improve flood depth predictions. Additionally, the study found that human interventions, such as embankment repairs, impacted flood depth estimations. By identifying and accounting for these factors, the RMSE values improved by approximately 0.05–0.1 m.

Furthermore, the iRIC flood simulations, which used various rainfall recurrence intervals, were compared with the outcomes from the third-generation flood hazard map provided by the Taiwan Water Resources Agency. Although there is not a substantial degree of alignment between the two sets of simulation results, the iRIC simulation grid for each recurrence interval is more detailed and includes the configuration of buildings and box culverts. Consequently, the simulation of flow conditions reflects the influence of nearby buildings and drainage infrastructure, thereby enhancing its ability to accurately represent the real flood scenario in areas with these structures.

In summary, this study demonstrates a feasible method for significantly improving the accuracy of flood depth estimation by using simulated flow data combined with detailed digital surface information. These insights can be applied worldwide to other interest areas with available flow data to enable more precise and effective flood depth predictions, which could strengthen flood management and disaster prevention.

Author Contributions: Conceptualization, Y.-P.H. and H.-P.T.; methodology, Y.-P.H.; software, Y.-P.H.; validation, Y.-P.H. and H.-P.T.; formal analysis, Y.-P.H. and H.-P.T.; investigation, Y.-P.H. and H.-P.T.; resources, H.-P.T.; data curation, Y.-P.H.; writing—original draft preparation, Y.-P.H. and H.-P.T.; writing—review and editing, H.-P.T. and L.-C.C.; visualization, Y.-P.H.; supervision, H.-P.T.; project administration, H.-P.T.; funding acquisition, H.-P.T. All authors have read and agreed to the published version of the manuscript.

Funding: This work was partially financially supported by the "Innovation and Development Center of Sustainable Agriculture" from The Featured Areas Research Center Program within the framework of the Higher Education Sprout Project by the Ministry of Education (MOE) in Taiwan. Additionally, support was also provided by the National Science and Technology Council under projects 111-2121-M-005-002-, 112-2321-B-005-007-, 112-2634-F-005-002-, 112-2119-M-005-001-, 112-2121-M-005-003-, and 112-2621-M-002-005-MY3.

Data Availability Statement: The Hydrologic Modeling System HEC-HMS is available at the Hydrologic Engineering Center.

Conflicts of Interest: The authors declare no conflict of interest.

References

1. Myhre, G.; Alterskjær, K.; Stjern, C.W.; Hodnebrog, Ø.; Marelle, L.; Samset, B.H.; Sillmann, J.; Schaller, N.; Fischer, E.; Schulz, M.; et al. Frequency of extreme precipitation increases extensively with event rareness under global warming. *Sci. Rep.* **2019**, *9*, 16063. [CrossRef]
2. Wang, B.; Biasutti, M.; Byrne, M.P.; Castro, C.; Chang, C.-P.; Cook, K.; Fu, R.; Grimm, A.M.; Ha, K.-J.; Hendon, H.; et al. Monsoons climate change assessment. *Bull. Am. Meteorol. Soc.* **2021**, *102*, E1–E19. [CrossRef]
3. Nyatuame, M.; Agodzo, S. Analysis of extreme rainfall events (drought and flood) over Tordzie Watershed in the Volta Region of Ghana. *J. Geosci. Environ. Prot.* **2017**, *5*, 275–295. [CrossRef]
4. Handwerger, A.L.; Huang, M.H.; Fielding, E.J.; Booth, A.M.; Bürgmann, R. A shift from drought to extreme rainfall drives a stable landslide to catastrophic failure. *Sci. Rep.* **2019**, *9*, 1569. [CrossRef]
5. Gioia, A.; Totaro, V.; Bonelli, R.; Esposito, A.A.; Balacco, G.; Iacobellis, V. Flood susceptibility evaluation on ephemeral streams of Southern Italy: A case study of Lama Balice. In Proceedings of the Computational Science and Its Applications–ICCSA 2018: 18th International Conference 2018, Melbourne, VIC, Australia, 2–5 July 2018; Proceedings, Part V 18; Springer International Publishing: Cham, Switzerland, 2018; pp. 334–348. [CrossRef]
6. Maxwell, S.L.; Butt, N.; Maron, M.; McAlpine, C.A.; Chapman, S.; Ullmann, A.; Segan, D.B.; Watson, J.E.M. Conservation implications of ecological responses to extreme weather and climate events. *Divers. Distrib.* **2019**, *25*, 613–625. [CrossRef]
7. Henny, L.; Thorncroft, C.D.; Hsu, H.H.; Bosart, L.F. Extreme rainfall in Taiwan: Seasonal statistics and trends. *J. Clim.* **2021**, *34*, 4711–4731. [CrossRef]
8. Dilley, M. *Natural Disaster Hotspots: A Global Risk Analysis*; World Bank Publications: Washington, DC, USA, 2005; Volume 5. [CrossRef]
9. Shiu, C.J.; Liu, S.C.; Chen, J.P. Diurnally asymmetric trends of temperature, humidity, and precipitation in Taiwan. *J. Clim.* **2009**, *22*, 5635–5649. [CrossRef]
10. Wu, Y.C.; Wang, S.Y.S.; Yu, Y.C.; Kung, C.Y.; Wang, A.H.; Los, S.A.; Huang, W.R. Climatology and change of extreme precipitation events in Taiwan based on weather types. *Int. J. Climatol.* **2019**, *39*, 5351–5366. [CrossRef]

11. Tseng, C.W.; Song, C.E.; Wang, S.F.; Chen, Y.C.; Tu, J.Y.; Yang, C.J.; Chuang, C.W. Application of high-resolution radar rain data to the predictive analysis of landslide susceptibility under climate change in the Laonong Watershed, Taiwan. *Remote Sens.* **2020**, *12*, 3855. [CrossRef]
12. Chen, Y.J.; Lin, H.J.; Liou, J.J.; Cheng, C.T.; Chen, Y.M. Assessment of flood risk map under climate change RCP8. 5 scenarios in Taiwan. *Water* **2022**, *14*, 207. [CrossRef]
13. Sahu, S.A.L.I.L.; Pyasi, S.K.; Galkate, R.V. A review on the HEC-HMS rainfall-runoff simulation model. *Int. J. Agric. Sci. Res.* **2020**, *10*, 183–190. [CrossRef]
14. Rai, P.K.; Dhanya, C.T.; Chahar, B.R. Coupling of 1D models (SWAT and SWMM) with 2D model (iRIC) for mapping inundation in Brahmani and Baitarani river delta. *Nat. Hazards* **2018**, *92*, 1821–1840. [CrossRef]
15. Kumar, S.; Agarwal, A.; Villuri, V.G.K.; Pasupuleti, S.; Kumar, D.; Kaushal, D.R.; Gosain, A.K.; Bronstert, A.; Sivakumar, B. Constructed wetland management in urban catchments for mitigating floods. *Stoch. Environ. Res. Risk Assess.* **2021**, *35*, 2105–2124. [CrossRef]
16. Zhang, K.; Shalehy, M.H.; Ezaz, G.T.; Chakraborty, A.; Mohib, K.M.; Liu, L. An integrated flood risk assessment approach based on coupled hydrological-hydraulic modeling and bottom-up hazard vulnerability analysis. *Environ. Model. Softw.* **2022**, *148*, 105279. [CrossRef]
17. Halwatura, D.; Najim, M.M.M. Application of the HEC-HMS model for runoff simulation in a tropical catchment. *Environ. Model. Softw.* **2013**, *46*, 155–162. [CrossRef]
18. Lin, Q.; Lin, B.; Zhang, D.; Wu, J. Web-based prototype system for flood simulation and forecasting based on the HEC-HMS model. *Environ. Model. Softw.* **2022**, *158*, 105541. [CrossRef]
19. Olayinka, D.; Irivbogbe, H. Estimation of Hydrological Outputs using HEC-HMS and GIS. *NJ Environ. Sci. Technol.* **2017**, *1*, 390–402. [CrossRef]
20. Janicka, E.; Kanclerz, J. Assessing the Effects of Urbanization on Water Flow and Flood Events Using the HEC-HMS Model in the Wirynka River Catchment, Poland. *Water* **2022**, *15*, 86. [CrossRef]
21. Liu, W.C.; Hsieh, T.H.; Liu, H.M. Flood risk assessment in urban areas of southern Taiwan. *Sustainability* **2021**, *13*, 3180. [CrossRef]
22. Hussain, F.; Wu, R.S.; Yu, K.C. Application of physically based semi-distributed hec-hms model for flow simulation in tributary catchments of kaohsiung area taiwan. *J. Mar. Sci. Technol.* **2021**, *29*, 4. [CrossRef]
23. Nelson, J.M.; Shimizu, Y.; Abe, T.; Asahi, K.; Gamou, M.; Inoue, T.; Iwasaki, T.; Kakinuma, T.; Kawamura, S.; Kimura, I.; et al. The international river interface cooperative: Public domain flow and morphodynamics software for education and applications. *Adv. Water Resour.* **2016**, *93*, 62–74. [CrossRef]
24. Shokory, J.A.N.; Tsutsumi, J.I.G.; Sakai, K. Flood modeling and simulation using iRIC: A case study of Kabul City. *E3S Web Conf.* **2016**, *7*, 04003. [CrossRef]
25. Dhanapala, L.; Gunarathna, M.H.J.P.; Kumari, M.K.N.; Ranagalage, M.; Sakai, K.; Meegastenna, T.J. Towards Coupling of 1D and 2D Models for Flood Simulation—A Case Study of Nilwala River Basin, Sri Lanka. *Hydrology* **2022**, *9*, 17. [CrossRef]
26. Kumar, A.; Khosa, R.; Gosian, A.K. A Framework for Assessment of Flood Conditions Using Hydrological and Hydrodynamic Modeling Approach. *Water* **2023**, *15*, 1371. [CrossRef]
27. Kojima, H.; Kogo, Y.; Shimada, K.; Shoda, D.; Suzuki, N. Inundation analysis of agricultural reservoirs destroyed by the 2011 off the Pacific coast of Tohoku earthquake. *Trans. Jpn. Soc. Agric. Rural Eng.* **2016**, *84*, I_93–I_101. [CrossRef]
28. Jamrussri, S.; Toda, Y. Simulating past severe flood events to evaluate the effectiveness of nonstructural flood countermeasures in the upper Chao Phraya River Basin, Thailand. *J. Hydrol. Reg. Stud.* **2017**, *10*, 82–94. [CrossRef]
29. El Fels, A.E.A.; Alaa, N.; Bachnou, A.; Rachidi, S. Flood frequency analysis and generation of flood hazard indicator maps in a semi-arid environment, case of Ourika watershed (western High Atlas, Morocco). *J. Afr. Earth Sci.* **2018**, *141*, 94–106. [CrossRef]
30. Savitri, A.; Budieny, H.; Bagaskara, F.; Lestari, F.M. Numerical Analysis in Dengkeng River Using Nays2DFlood. *Civ. Eng. Archit.* **2020**, *8*, 533–540. [CrossRef]
31. Uwineza, A.; Irie, M. Flood analysis for estimating the impact of rainwater harvesting system installation using hydrological models. Case study: Nyabugogo valley, Kigali. *J. Arid Land Stud.* **2022**, *32*, 145–149. [CrossRef]
32. Takayama, R.; Nakamura, R.; Esteban, M.; Mäll, M.; Ohizumi, K. Pseudo global warming experiment of flood inundation in the upper White Volta River, Ghana. *J. Hydrol. Reg. Stud.* **2023**, *45*, 101297. [CrossRef]
33. Wing, O.E.; Bates, P.D.; Sampson, C.C.; Smith, A.M.; Johnson, K.A.; Erickson, T.A. Validation of a 30 m resolution flood hazard model of the conterminous U nited S tates. *Water Resour. Res.* **2017**, *53*, 7968–7986. [CrossRef]
34. Ward, P.J.; Jongman, B.; Salamon, P.; Simpson, A.; Bates, P.; De Groeve, T.; Muis, S.; de Perez, E.C.; Rudari, R.; Trigg, M.A.; et al. Usefulness and limitations of global flood risk models. *Nat. Clim. Change* **2015**, *5*, 712–715. [CrossRef]
35. Polat, N.; Uysal, M. DTM generation with UAV based photogrammetric point cloud. *Int. Arch. Photogramm. Remote Sens. Spat. Inf. Sci.* **2017**, *42*, 77–79. [CrossRef]
36. Arif, F.; Maulud, K.A.; Ab Rahman, A.A. Generation of digital elevation model through aerial technique. *IOP Conf. Ser. Earth Environ. Sci.* **2018**, *169*, 012093. [CrossRef]
37. Manfreda, S.; McCabe, M.F.; Miller, P.E.; Lucas, R.; Madrigal, V.P.; Mallinis, G.; Ben Dor, E.; Helman, D.; Estes, L.; Ciraolo, G.; et al. On the use of unmanned aerial systems for environmental monitoring. *Remote Sens.* **2018**, *10*, 641. [CrossRef]
38. Annis, A.; Nardi, F.; Petroselli, A.; Apollonio, C.; Arcangeletti, E.; Tauro, F.; Belli, C.; Bianconi, R.; Grimaldi, S. UAV-DEMs for small-scale flood hazard mapping. *Water* **2020**, *12*, 1717. [CrossRef]

39. Utlu, M.; Özdemir, H. How much spatial resolution do we need to model a local flood event? Benchmark testing based on UAV data from Biga River (Turkey). *Arab. J. Geosci.* **2020**, *13*, 1293. [CrossRef]
40. Kim, S.; Lee, S.; Kim, T.W.; Kim, D. Estimation of flooded area using satellite imagery and DSM Terrain data. *J. Korean Soc. Hazard Mitig.* **2019**, *19*, 471–483. [CrossRef]
41. Su, Y.F.; Lin, Y.T.; Jang, J.H.; Han, J.Y. High-Resolution Flood Simulation in Urban Areas Through the Application of Remote Sensing and Crowdsourcing Technologies. *Front. Earth Sci.* **2022**, *9*, 756198. [CrossRef]
42. Moriasi, D.N.; Arnold, J.G.; Van Liew, M.W.; Bingner, R.L.; Harmel, R.D.; Veith, T.L. Model evaluation guidelines for systematic quantification of accuracy in watershed simulations. *Trans. ASABE* **2007**, *50*, 885–900. [CrossRef]
43. Shimizu, Y.; Inoue, T.; Suzuki, E.; Kawamura, S.; Iwasaki, T.; Hamaki, M.; Yoshida, T. *Nays2D Flood Solver Manual*; The International River Interface Cooperative (iRIC): Hokkaido, Japan, 2015; pp. 1–51.
44. Tassew, B.G.; Belete, M.A.; Miegel, K. Application of HEC-HMS model for flow simulation in the Lake Tana basin: The case of Gilgel Abay catchment, upper Blue Nile basin, Ethiopia. *Hydrology* **2019**, *6*, 21. [CrossRef]
45. Coveney, S.; Roberts, K. Lightweight UAV digital elevation models and orthoimagery for environmental applications: Data accuracy evaluation and potential for river flood risk modelling. *Int. J. Remote Sens.* **2017**, *38*, 3159–3180. [CrossRef]